



Damping of surface waves by a floating viscoplastic plateXuemeng Wang  and Neil J. Balmforth *Department of Mathematics, University of British Columbia, Vancouver, British Columbia, Canada V6T 1Z2*

(Received 29 September 2022; accepted 23 November 2022; published xxxxxxxxx)

A theoretical model is presented to explore how surface waves in an inviscid fluid layer are damped by the bending stresses induced in a overlying floating film of yield-stress fluid. The model applies in the long-wavelength limit, combining the shallow-water equations for the inviscid fluid with a theory for the bending of a thin viscoplastic plate described by the Herschel-Bulkley constitutive law. An exploration of the energetics captured by the model suggests that waves decay to rest in finite time, a result that is confirmed using a combination of approximate, numerical and asymptotic solutions to the model equations. In the limit that the plate behaves like a perfectly plastic material, the sloshing motions take the form of triangular waves with bending restricted to narrow viscoplastic hinges.

DOI: [10.1103/PhysRevFluids.00.003300](https://doi.org/10.1103/PhysRevFluids.00.003300)**I. INTRODUCTION**

The damping of surface waves by floating material plays an important role in geophysics and engineering. In the marginal ice zone, for example, broken floating ice damps sea waves, with important implications on the maintenance of ice cover and the Arctic climate [1,2]; the old adage “pouring oil on troubled waters” stems from the notion of calming wave motion by floating a viscous fluid film on the surface [3,4], and sloshing in liquid filled containers can be mitigated by foam to limit flooding and damage [5,6].

To explore experimentally how floating particles affected wave motion, Sutherland and Balmforth [7] examined how layers of floating hydrogel spheres damped sloshes in a rectangular tank. At larger amplitudes, it was found that the particles contributed to the familiar exponential damping arising from viscous boundary layers along the sides of the tank. But for lower amplitudes, wave motion was damped more strongly by the pack of particles, bringing sloshes to rest in finite time. This nonlinear effect was attributed to the jamming of the particles as they were brought together during certain phases of the slosh cycle. A similar nonlinear damping was subsequently observed by Kalinichenko [8], who studied the effect of floating particles of polystyrene on surface waves. The nonlinear dynamics of a moving contact line has also been shown to arrest sloshing motion in finite time [9–12].

The purpose of the present article is to consider theoretically the effect of a floating viscoplastic film on wave motion. When the film is relatively stiff, one expects that the waves chiefly deform that “plate” by bending, without significant thinning. This scenario is the viscoplastic analog of wave propagation under an elastic beam, theoretical models for which have been proposed previously for ice-covered ocean [1,2]. With a classical Euler-Bernoulli beam, the main effect is to alter the dispersion relation of low-amplitude water waves [2], although linear (exponential) damping can also be introduced by generalizing the model to a viscoelastic beam [13].

For a viscoplastic beam, the bending stresses stemming from a constant viscosity likely contribute to any exponential damping, whereas the yield stress introduces the possibility of a transition to a rigid state, or jamming. Thus, one anticipates that some of the features observed experimentally for floating hydrogel may be captured in a model in which the sloshing of a water layer is resisted by

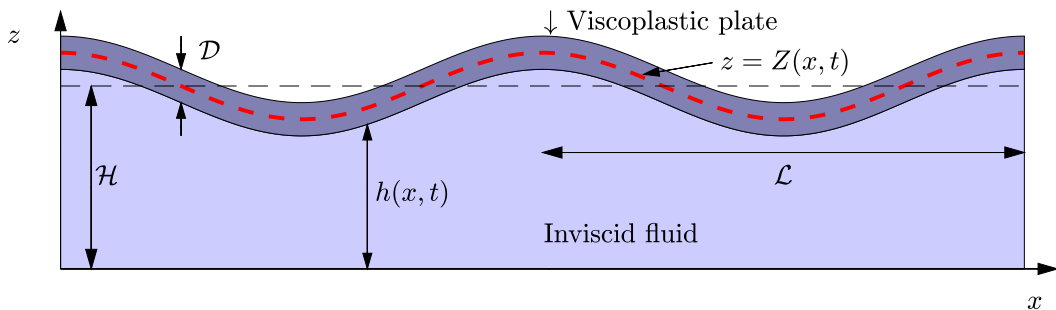


FIG. 1. Sketch of the geometry.

43 a floating viscoplastic plate. Since foams are also sometimes described by viscoplastic constitutive
 44 laws [14], this type of model may also apply to sloshing problems with floating foam [5].

45 To formulate a relatively simple model, we consider a shallow layer of water below a thin viscoplastic
 46 plate. In particular, in this limit, we couple the classical shallow-water equations [15] with
 47 the viscoplastic plate model derived by Balmforth and Hewitt [16]. The latter is derived from the
 48 governing equations of a yield stress fluid in the thin-plate limit, incorporating the Herschel-Bulkley
 49 constitutive law to describe the rheology [17]. The full three-dimensional version of this model [18]
 50 combines the effects of bending and tension, and therefore provides the viscoplastic analog of the
 51 Föppl–von Kármán plate equations, bridging between viscous sheet models [19–21] and classical
 52 theories of plastic plates [22–24]. For the present task, however, we do not need the full machinery
 53 of this model, and use a reduction of it, suitable for low-amplitude two-dimensional waves in which
 54 only bending is important. Our goal is to explore how the nonlinear viscosity and yield stress of
 55 the Herschel-Bulkley constitutive law affect wave damping, and to confirm that the latter can arrest
 56 motion in finite time. In an Appendix, we remove the restriction that the water layer is shallow, and
 57 consider the effect of the viscoplastic bending stresses on irrotational surface waves.

58 II. MODEL EQUATIONS

59 A. Governing equations

60 We model a thin plate of viscoplastic fluid satisfying the Herschel-Bulkley constitutive law lying
 61 above a shallow layer of inviscid fluid, as sketched in Fig. 1. Both fluids are incompressible. The
 62 thickness D of the plate is comparable to the typical depth of the inviscid fluid layer \mathcal{H} . Both are
 63 much smaller than the characteristic lengthscale \mathcal{L} over which the plate bends, or, equivalently, that
 64 characterizes depth variations of the inviscid fluid layer:

$$\epsilon = \frac{\mathcal{H}}{\mathcal{L}} \ll 1, \quad \delta = \frac{D}{\mathcal{H}} = O(1). \quad (1)$$

65 We use a Cartesian coordinate system (x, z) to describe the geometry, where the z axis points verti-
 66 cally upwards, opposite to gravity, with acceleration g . The governing equations for incompressible
 67 fluid with velocity field $\mathbf{u} = (u, w)$ are

$$\nabla \cdot \mathbf{u} = 0, \quad (2)$$

$$\rho \left(\frac{\partial \mathbf{u}}{\partial t} + \mathbf{u} \cdot \nabla \mathbf{u} \right) = -\nabla p + \nabla \cdot \boldsymbol{\tau} - \rho g \hat{\mathbf{z}}, \quad (3)$$

68 where ρ denotes the density of each fluid, p is pressure, and $\boldsymbol{\tau}$ is the deviatoric stress tensor. In
 69 the inviscid fluid, we discard the deviatoric stresses τ_{jk} , but for the plate, the Herschel-Bulkley

constitutive law provides the relations

$$\begin{aligned} \dot{\boldsymbol{\gamma}} &= \mathbf{0}, & \tau < \tau_Y, \\ \boldsymbol{\tau} &= \left(K \dot{\boldsymbol{\gamma}}^{n-1} + \frac{\tau_Y}{\dot{\boldsymbol{\gamma}}} \right) \dot{\boldsymbol{\gamma}}, & \tau \geq \tau_Y, \end{aligned} \quad (4)$$

where τ_Y , K , and n represent the yield stress, consistency, and power-law index, and

$$\dot{\gamma}_{jk} = \frac{\partial u_j}{\partial x_k} + \frac{\partial u_k}{\partial x_j}, \quad \dot{\boldsymbol{\gamma}} = \sqrt{\frac{1}{2} \sum_{j,k} \dot{\gamma}_{jk}^2}, \quad \tau = \sqrt{\frac{1}{2} \sum_{j,k} \tau_{jk}^2}. \quad (5)$$

For $\tau_Y \rightarrow 0$ and $n \rightarrow 1$, the Herschel-Bulkley law reduces to that for a viscous fluid.

The densities of the viscous fluid and plate are not necessarily the same; $\rho = \rho_f$ denotes the density of the inviscid fluid, whereas $\rho = \rho_p$ is that of the plate. At the interface between the two fluids, $z = h(x, t)$, we apply the usual kinematic condition and demand that stresses are continuous, ignoring any interfacial tension.

B. Shallow water theory for the inviscid fluid

Because the fluid layer underneath the plate is relatively shallow, we exploit the shallow-water approximation to describe the flow dynamics. In this approximation, the vertical pressure gradient becomes hydrostatic, so that

$$p(x, t) = \rho_f g(h - z) + P(x, t), \quad (6)$$

where $P(x, t)$ denotes the confining pressure due to the plate. The flow speed $u(x, t)$ is also independent of depth, and conservation of mass and momentum reduce to the shallow-layer equations

$$h_t + (hu)_x = 0, \quad (7)$$

$$\rho_f (u_t + uu_x) = -\rho_f gh_x - P_x, \quad (8)$$

where the subscripts x and t denote partial derivatives.

C. Viscoplastic plate model

Pressures built up underneath the plate force that skin to bend. As shown previously [16,18], provided the plate is thin, the local thickness \mathcal{D} does not change to leading order, and a combination of bending stresses and in-plane tensions oppose deformation. Thus, the centerline of the plate lies at $Z = \frac{1}{2}\mathcal{D} + h$, and $W = Z_t = h_t$ denotes the vertical plate velocity.

The main thrust of the earlier reductions [16,18] is to formulate vertically integrated equations of motion for the plate, together with constitutive relations for the bending moment and in-plane tension that oppose the imposed stresses, all descending from the original governing equations and Herschel-Bulkley law. When wave amplitudes remains sufficiently small that significant tensions are not generated, only the bending moment M acts, and conservation of vertical momentum demands

$$\rho_p \mathcal{D} \frac{\partial W}{\partial t} = \frac{\partial^2 M}{\partial x^2} + P + \rho_p g \mathcal{D}. \quad (9)$$

The constitutive law for M is given by

$$M = - \left(\frac{K \mathcal{D}^{n+2}}{n+2} |W_{xx}|^n + \frac{1}{2} \mathcal{D}^2 \tau_Y \right) \text{sgn}(W_{xx}), \quad (10)$$

if $|M| \geq \frac{1}{2} \mathcal{D}^2 \tau_Y$, with $W_{xx} = 0$ otherwise.

D. Dimensionless model equations

We now remove the dimensions from the equations by defining new variables, based on the natural scales characterizing motion in the shallow water layer, or the stress experienced when the plate bends, assuming that vertical displacements are of order of the plate thickness:

$$\tilde{t} = \frac{\mathcal{C}t}{\mathcal{L}} = \frac{\mathcal{V}t}{\mathcal{D}}, \quad \tilde{x} = \frac{x}{\mathcal{L}}, \quad h = \mathcal{H} + \mathcal{D}\eta, \quad Z = \mathcal{H} + \frac{1}{2}\mathcal{D} + \mathcal{D}\eta \quad (11)$$

and

$$\tilde{u} = \frac{\mathcal{H}u}{\mathcal{D}\mathcal{C}}, \quad \tilde{W} = \frac{W}{\mathcal{V}}, \quad \tilde{M} = \frac{M}{\mathcal{D}^2\mathcal{P}}, \quad \tilde{P} = \frac{\mathcal{L}^2}{\mathcal{P}\mathcal{D}^2}(P + \rho_r g\mathcal{D}), \quad (12)$$

where

$$\mathcal{P} = K\left(\frac{\mathcal{D}\mathcal{V}}{\mathcal{L}^2}\right)^n, \quad \mathcal{C} = \frac{\mathcal{L}\mathcal{V}}{\mathcal{D}} = \sqrt{g\mathcal{H}}. \quad (13)$$

Here \mathcal{C} is the natural wave speed of surface gravity waves on the shallow-water layer, which are associated with vertical motions of scale $\mathcal{V} = \mathcal{D}\mathcal{C}/\mathcal{L}$. The stress scale \mathcal{P} characterizes the bending of the plate, which translates to a bending moment of order $\mathcal{D}^2\mathcal{P}$ and must counter a normal load of $O(\mathcal{P}\mathcal{D}^2/\mathcal{L}^2)$ in the thin-plate limit [16,18]. For standing waves, we take \mathcal{L} to be set by the horizontal wavelength (so that $0 \leq x \leq 2\pi$). In addition to the power-law index n and depth ratio δ , we are then left with two other dimensionless groups (assumed order one):

$$S = \frac{\mathcal{P}\mathcal{D}}{\rho_f g\mathcal{L}^2} \quad \text{and} \quad \text{Bi} = \frac{\tau_y}{\mathcal{P}} = \frac{\tau_y}{K}\left(\frac{\mathcal{L}^2}{\mathcal{D}\mathcal{V}}\right)^n, \quad (14)$$

which compare the bending stress scale to the forces of inertia or gravity in the inviscid fluid, and the yield stress to the (nonlinear) viscous bending stresses.

After dropping the tilde decoration on the new variables, the dimensionless version of the model can then be written as

$$\eta_t = Z_t = W, \quad (15)$$

$$\eta_t + u_x + \delta(\eta u)_x = 0, \quad (16)$$

$$u_t + \delta u u_x = -S P_x - \eta_x, \quad (17)$$

$$0 = M_{xx} + P, \quad (18)$$

along with

$$M = -[(n+2)^{-1}|W_{xx}|^n + \frac{1}{2}\text{Bi}]\text{sgn}(W_{xx}), \quad (19)$$

for $|M| \geq \frac{1}{2}\text{Bi}$, implying that the plate is yielded. If $|M| < \frac{1}{2}\text{Bi}$, on the other hand, and the plate is rigid, then $W_{xx} = 0$. The constitutive law in (19) is illustrated in Fig. 2 for a Bingham plate ($n = 1$) and a power-law plate with $n = \frac{5}{3}$ and $\text{Bi} = 0$. Note that the vertical inertial term in (18) is discarded because it becomes $O(\epsilon^2\delta) \ll 1$ for $S = O(1)$.

E. Periodic waves in the quasilinear limit

If we now consider waves that are spatially periodic with wavelength \mathcal{L} , in the limit $\delta = \mathcal{D}/\mathcal{H} \rightarrow 0$, the nonlinear terms become deleted from the shallow-water part of the model to leave the ‘‘quasilinear’’ system,

$$\eta_{tt} = W_t = \eta_{xx} - S M_{xxxx}, \quad (20)$$

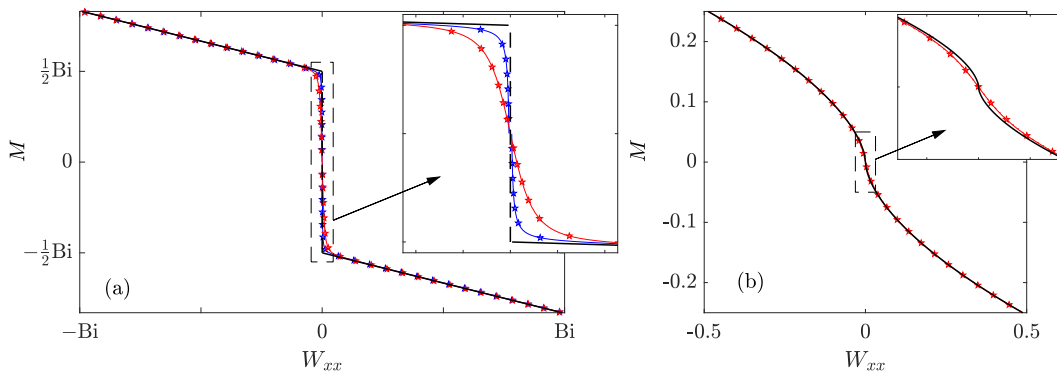


FIG. 2. An illustration of the constitutive law (19) for the bending moment M . In (a), we plot the (discontinuous) law for $\text{Bi} = \frac{1}{2}$ and $n = 1$ along with its regularizations in (31) (red with stars; $\varepsilon = 0.01$) and (32) (blue with stars; $\varepsilon = 0.02$). The power-law model with $n = \frac{3}{5}$ and $\text{Bi} = 0$ is plotted in (b), with its regularization for $\varepsilon = 0.01$ (red line and stars). The insets show magnifications at low shear rates; for that in (a), the unregularized law converges to the step, $-\frac{1}{3}\text{Bi} \text{sgn}(W_{xx})$, corresponding to the perfectly plastic limit.

together with (19). For the initial condition, we set

$$\eta(x, 0) = 0, \quad \text{and} \quad W(x, 0) = A_0 \sin x, \quad (21)$$

where the parameter $A_0 > 0$ gauges the initial wave amplitude relative to the plate thickness. We then look for spatially periodic, standing wave solutions over the interval $0 \leq x \leq 2\pi$. However, the spatial symmetries inherent in the model then imply that $\eta(x, t) = \eta(\frac{1}{2}\pi - x, t)$ and $\eta(x, t) = -\eta(x + \pi, t)$ for $0 \leq x \leq \frac{1}{2}\pi$. Consequently, some simplifications are implied in computations, and the model also applies to domains with either Dirichlet boundary conditions at $x = 0$ and π , or Neumann conditions at $x = \pm\frac{1}{2}\pi$.

Note that the model in (19)–(21) can be further rescaled to eliminate one of the parameters: if we define $(\hat{\eta}, \hat{W}) = A_0^{-1}(\eta, W)$, $\hat{S} = A_0^{n-1}S$ and $\hat{\text{Bi}} = A_0^{-n}\text{Bi}$, then A_0 is removed in favour of the two new parameters \hat{S} and $\hat{\text{Bi}}$. Practically, we avoid this final notational change, noting that it chiefly implies that increases in the parameter A_0 are equivalent to decreases in Bi (our main concern below is with the Bingham plate, with $n = 1$).

Equation (21) implies an initial bending moment with

$$|M(x, 0)| = (n + 2)^{-1} A_0^n |\sin x|^n + \frac{1}{2} \text{Bi}. \quad (22)$$

Thus, the initial condition demands that the plate is immediately held above the yield stress everywhere but for the points $x = 0$ and π . When $\text{Bi} > 0$, one expects that rigid plugs develop about these points at later times as the surrounding bending moment decreases.

For a viscous plate, with $n = 1$ and $\text{Bi} = 0$, the solution is given immediately by

$$\eta(x, t) = \frac{A_0}{\omega} e^{-\frac{1}{6}S t} \sin \omega t \sin x, \quad \omega = \sqrt{1 - \frac{S^2}{36}}. \quad (23)$$

With $S = 0$, we recover the shallow-water sloshing solution $\eta(x, t) = \sin t \sin x$. For $S > 0$, the slosh becomes damped by viscous bending stresses; when $S > 6$, the slosh becomes overdamped.

F. Energetics

The quasilinear system possesses an associated energy equation,

$$\frac{d}{dt} \int_0^{2\pi} \frac{1}{2} (u^2 + \eta^2) dx = S \int_0^{2\pi} M W_{xx} dx = -S \int_0^{2\pi} \left[(n + 2)^{-1} |W_{xx}|^n + \frac{1}{2} \text{Bi} \right] |W_{xx}| dx, \quad (24)$$

142 obtained by multiplying (20) by $\phi(x, t)$ and integrating over a spatial period, where $u = \phi_x$ (or
 143 $\eta_t = -\phi_{xx}$). Thus, the potential and kinetic energies of the inviscid fluid layer are dissipated by
 144 bending stresses in the plate. In particular, in view of the quadratic form of the energy, one expects
 145 that viscous bending (described by the first term on the left of (24) with $n = 1$, and which is also
 146 quadratic) leads to exponential decay, but the plastic bending stress introduces a linear-in-time decay
 147 of the wave amplitude, i.e., the arrest of motion in finite time. If $n < 1$, even the power-law viscous
 148 contribution leads to faster-than-exponential decay.

149 Were the solution to remain of the form

$$\eta(x, t) = A(t) \sin x, \quad W(x, t) = \dot{A} \sin x, \quad (25)$$

150 even when in the presence of the plate, then (24) implies that

$$\frac{1}{2} \pi \frac{d}{dt} (A^2 + \dot{A}^2) = -\mathcal{S} [2(n+2)^{-1} \beta |\dot{A}|^n + 2\text{Bi}] |\dot{A}|, \quad (26)$$

151 where

$$\beta = \frac{1}{2} \int_0^{2\pi} |\sin x|^{n+1} dx \equiv \text{B} \left(\frac{1}{2}, \frac{1}{2}n + 1 \right)$$

152 denotes a beta function.

153 When the damping is relatively weak ($\mathcal{S} \ll 1$), the wave largely oscillates at the original
 154 frequency, with $A \approx a(t) \sin t$, where a is a slower function of time. Hence the left-hand side is
 155 approximately $\pi a \dot{a}$, and averaging the right-hand side over the fast oscillation then gives

$$\dot{a} \approx -\mathcal{S} \left[\frac{2\beta^2 |a|^n}{\pi^2(n+2)} + \frac{4\text{Bi}}{\pi^2} \right] \text{sgn}(a). \quad (27)$$

156 For $n = 1$, the viscous bending term reduces to $-\frac{1}{6} \mathcal{S} a$, giving a decay rate in agreement with (23).
 157 As noted above, the plastic bending moment prompts a final linear decay that ends in finite time;
 158 the associated stopping time is

$$t_s = \frac{6}{\mathcal{S}} \log \left(1 + \frac{\pi^2 A_0}{24\text{Bi}} \right). \quad (28)$$

159 With $n < 1$ and $\text{Bi} = 0$, the power-law viscous contribution leads to the solution,

$$a \approx A_0 \left(1 - \frac{t}{t_s} \right)^{\frac{1}{1-n}}, \quad t_s = \frac{\pi^2 A_0^{1-n} (2+n)}{2\beta^2 \mathcal{S} (1-n)}. \quad (29)$$

160 The preceding results must be viewed with some caution, however, as the bending stresses modify
 161 the form of the solution in (25). In particular, as we demonstrate below in Sec. III by numerically
 162 solving the model equations, these stresses create unyielded plugs over parts of the plate [where
 163 $W_{xx} = 0$ and (25) can no longer apply]. Nevertheless, the relatively high derivatives associated with
 164 viscous bending over the yielded regions imply that higher Fourier modes are much more strongly
 165 damped there than the gravest mode in (25). Consequently, the approximation in (26) works well in
 166 reproducing numerical solutions, as we shall see below in Sec. III.

167 G. Computational method

168 For $n = 1$, the constitutive law becomes more transparent:

$$M = -\frac{1}{3} W_{xx} - \frac{1}{2} \text{Bi} \text{sgn}(W_{xx}), \quad \text{for } |M| \geq \frac{1}{2} \text{Bi} \quad (\text{and } W_{xx} = 0 \text{ otherwise}). \quad (30)$$

169 To ease analysis, this law may be regularized with the replacement,

$$M = -\frac{1}{2} W_{xx} \left(1 + \frac{3\text{Bi}}{2\sqrt{\varepsilon^2 + W_{xx}^2}} \right), \quad (31)$$

for some regularization parameter $\varepsilon \ll 1$. This sets the stage for a relatively straightforward numerical exploration of the quasilinear model in which a finite grid can be adopted in x and spectral differentiation matrices [25] used to evaluate spatial derivatives. The resulting ordinary differential equations (ODEs) can then be integrated in time using a stiff integrator, following the usual method of lines (practically, we use Matlab's ODE15s). The regularization of the constitutive law in (31) is key to this algorithm, as the switches in the original constitutive law imply that the smoothness of the solution becomes lost at any yield points, limiting the convergence of any Fourier series representation of the solution. Practically, we use a grid of 64 or 128 points and $\varepsilon = 10^{-4}$ or lower, and have verified that the solutions are not sensitive either to the precise number of grid points or the value of ε .

Alternatively, the model equations can be attacked by replacing W_t in (24) by a centered difference after discretizing in time with a suitably small time step Δt . The resulting spatial boundary-value problem can then be solved using Matlab's BVP4c. In this algorithm, the bending moment becomes one of the dependent variables in the BVP4c solution, and we employ the alternative, regularized constitutive law,

$$W_{xx} = -\frac{3}{2} \left[|M| - \frac{1}{2} \text{Bi} + \sqrt{\left(|M| - \frac{1}{2} \text{Bi} \right)^2 + \varepsilon^2} \right] \text{sgn}(M). \quad (32)$$

The main limitation is now to maintain the accuracy of the solution by taking Δt to be sufficiently small; the regularization parameter can be taken to be very small (with BVP4c selecting an adaptive spatial grid to ensure spatial accuracy). Practically, we use $\Delta t = 10^{-4}$ and $\varepsilon = 10^{-6}$, again verifying that the solution is insensitive to those precise values. The two schemes provide equivalent results; the spectral algorithm is faster and more accurate in time integration, whereas the boundary-value solver performs better in resolving any finer spatial features. We report results using the spectral scheme.

For a power-law plate with $\text{Bi} = 0$, we again use the spectral method with 128 grid points, regularizing the constitutive law by replacing $|W_{xx}|^{n-1}$ by $(W_{xx}^2 + \varepsilon^2)^{\frac{n-1}{2}}$. In this case, and take ε to be 10^{-8} or smaller. The various regularized versions of the constitutive model, and how well they reproduce the original discontinuous constitutive model (19) (for somewhat larger values of the regularization parameter ε), are illustrated in Fig. 2.

III. RESULTS

A. Approximate solution

For $n = 1$, the approximation in (26) can be written as the relatively simple ODE,

$$\ddot{A} + A + \frac{1}{3} \mathcal{S} \dot{A} + \frac{2\mathcal{S}\text{Bi}}{\pi} \text{sgn}(\dot{A}) = 0, \quad (33)$$

which is linear but for the switches at the sign changes of \dot{A} . At such a change of sign, the rate of change \dot{A} predicted by (33) must be consistent with the associated increase or decrease of \dot{A} , a condition that demands that $|A|$ exceeds $2\mathcal{S}\text{Bi}/\pi$ at this instant. If, however, $|A| < 2\mathcal{S}\text{Bi}/\pi$ at this moment, the solution cannot be continued consistently. Instead, the solution must reach an unyielded state. The cessation of motion therefore arises at the first instant,

$$t = t_s(\mathcal{S}, \text{Bi}, A_0) \approx (2j - 1) \frac{\pi}{\omega}, \quad j = 1, 2, \dots, \quad (34)$$

that $\dot{A}(t_s) = 0$ and $|A(t_s)| < 2\mathcal{S}\text{Bi}/\pi$. This cessation leaves a residual value for $A(t)$ which corresponds to a frozen slosh of the plate. Sample solutions to (33) for $\mathcal{S} = \text{Bi} = \frac{1}{2}$ and different values of A_0 are illustrated in Fig. 3. The final amplitude $A(t_s)$ and cessation time t_s are displayed as a function of A_0 in Fig. 4 for $\mathcal{S} = \text{Bi} = \frac{1}{2}$. As the initial amplitude increases, the slosh is able to continue through more and more oscillations, with the cessation conditions leading to the stopping

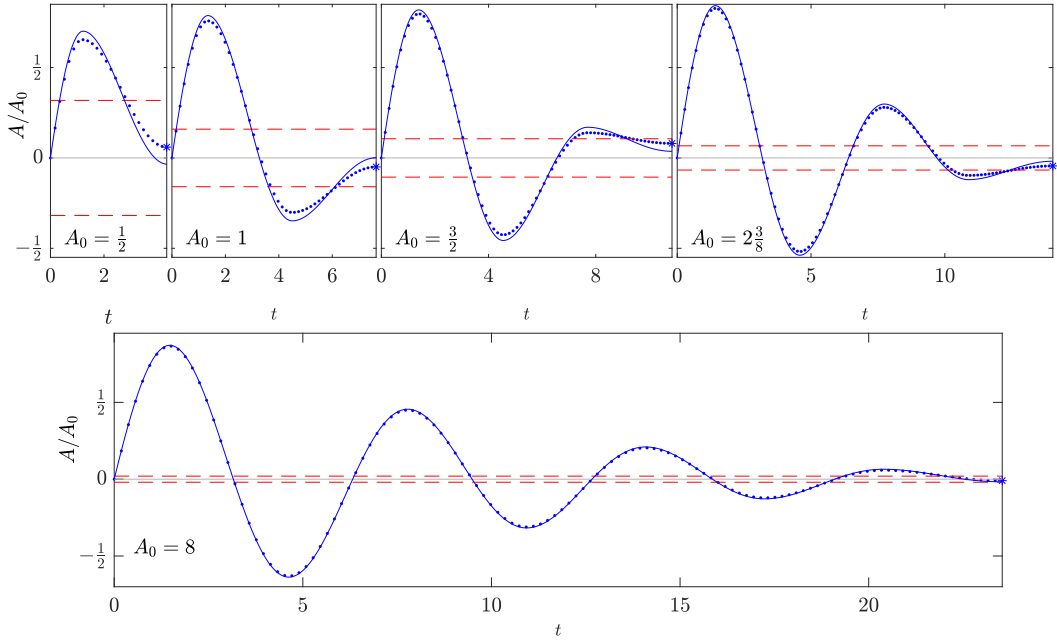


FIG. 3. Approximate solutions, $A(t)/A_0$, computed using (33) for $S = \text{Bi} = \frac{1}{2}$, $n = 1$, and the values of A_0 indicated (dotted lines). The limits $\pm 2S\text{Bi}/\pi$ are indicated by the dashed lines and the star indicates the cessation of motion. The solid lines show $\eta(\frac{1}{2}\pi, t)$ from corresponding numerical results using (19)–(21) (with $n = 1$). (The faint gray line shows the time axis.)

210 time increasing through a sequence of steps, and the final amplitude passing through sawtooth-like
 211 oscillations. The overall lengthening of the stopping time with increasing initial amplitude (but not
 212 the steps) is captured by the small-damping prediction in (28).

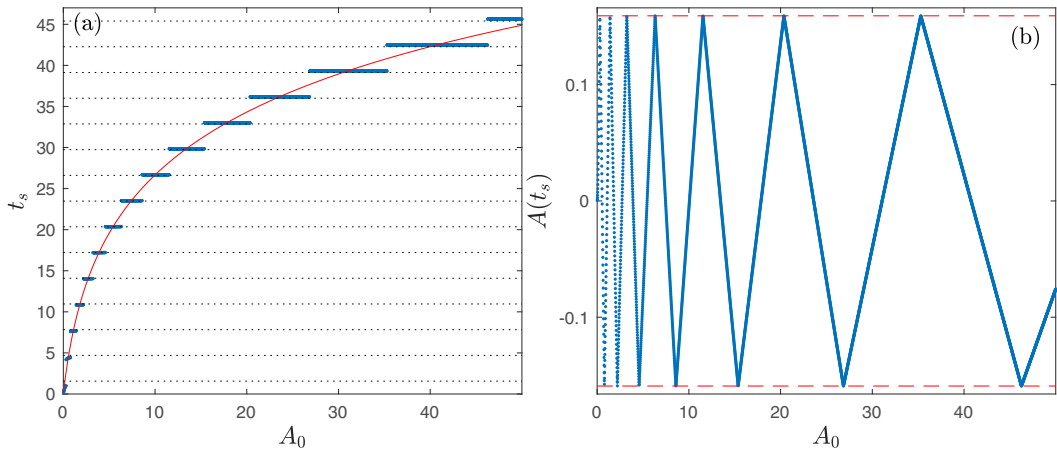


FIG. 4. Approximate stopping times and final amplitudes, t_s and $A(t_s)$, against initial amplitude A_0 , using (33) and $S = \text{Bi} = \frac{1}{2}$. The small damping prediction (28) and the limits $\pm 2S\text{Bi}/\pi$ are indicated by the solid and dashed lines, respectively. In (a) the horizontal dotted lines show (34).

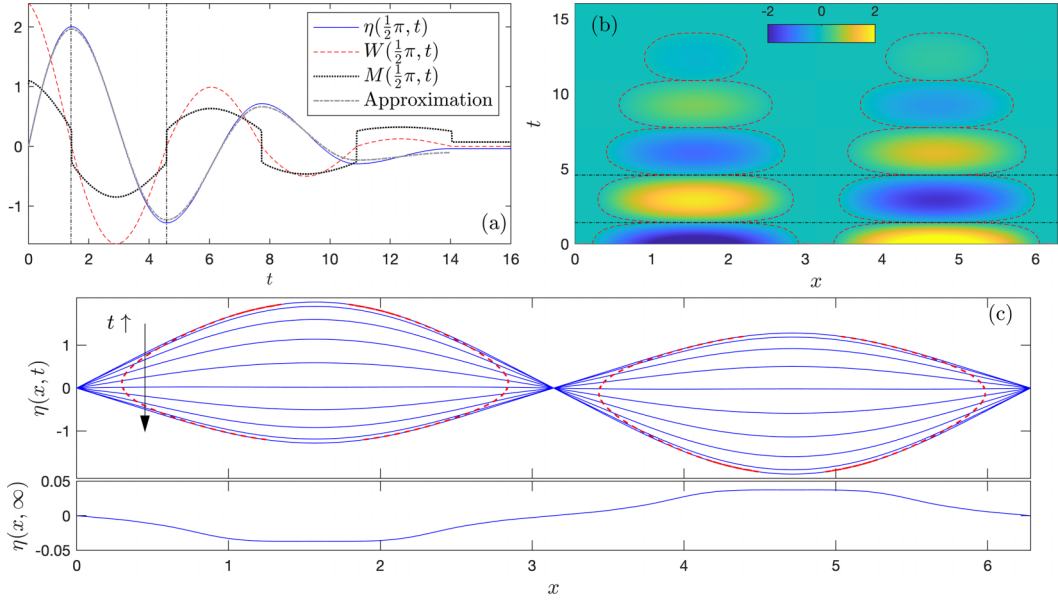


FIG. 5. Sample solution for $S = \text{Bi} = \frac{1}{2}$, $n = 1$ and $A_0 = \frac{19}{8}$, showing (a) time series of η , W and M at $x = \frac{1}{2}\pi$, (b) the curvature rate $W_{xx}(x, t)$ as a density plot on the (x, t) plane, and (c) ten equally spaced snapshots of $\eta(x, t)$ between the first extrema of $\eta(\frac{1}{2}\pi, t)$ [occurring at the instants indicated by the dot-dashed lines in (a) and (b)] along with the residual plate shape $\eta(x, \infty)$. In (a) the dots show the corresponding prediction from (33). The locus of the yield points are shown by the dashed lines in (b) and (c).

B. Numerical results for a Bingham plate

A sample numerical solution for a Bingham plate ($n = 1$) is displayed in Fig. 5. As suggested by the approximate model, the bending stresses in the plate damp the slosh, which passes through two decaying oscillations before coming to rest in finite time. The dynamics is more complicated than captured by the approximate solution, however: the points at $x = 0, \pi, \dots$, expand immediately into plugged sections of the plate whose borders vary with time. The shape of the plate therefore deviates from the sinusoidal form in (25) and the final state becomes more complicated, depending on the history of the plugs. Despite this, the prediction from (33) performs surprising well in reproducing the amplitude, extracted as $\eta(\frac{1}{2}\pi, t)$ (see also Fig. 3).

As in the approximate solution, sloshing ceases when the oscillation passes through a node [in $W(\frac{1}{2}\pi, t)$] and the hydrostatic pressure gradient in the lower layer [described by the term η_{xx} in (20)] is not sufficient to restart motion. This again leads to a steplike dependence of the stopping time t_s on initial amplitude (Fig. 6). The evolving spatial structure in the full problem, however, renders the approximation in (33) a qualitative, but not quantitative, guide to the stopping time and final amplitude; see Fig. 6.

The dynamics for other parameter settings are largely similar to that illustrated in Fig. 5. However, for large S or Bi (or small A_0), the plate returns to rest without passing through an oscillation (e.g., Fig. 7). In the weakly damped limit, $S \ll 1$ and $(A_0, \text{Bi}) = O(1)$, on the other hand, the oscillations are prolonged, as illustrated in Fig. 8.

C. Plastic limit

For $S \rightarrow 0$ with $S\text{Bi} = O(1)$, the plate approaches a perfectly plastic limit in which the yield stress makes the only contribution to bending over the bulk of the plate [the limit of the constitutive law (19) illustrated in the inset of Fig. 2(a)], and viscous bending effects become localized to narrow

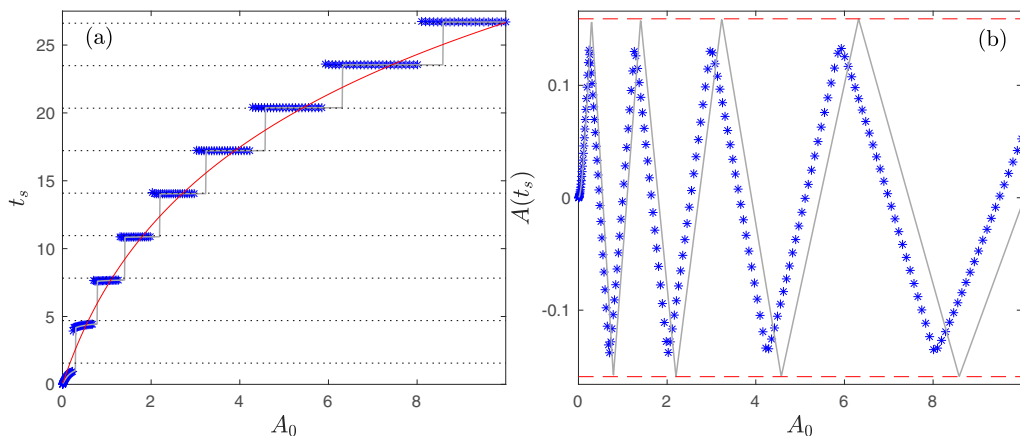


FIG. 6. Stopping times, t_s , and final amplitudes, $\eta(\frac{1}{2}\pi, t_s)$, against A_0 for $\mathcal{S} = \text{Bi} = \frac{1}{2}$ and $n = 1$. The thicker gray lines show the results from Fig. 4. The small damping prediction (28) and the limits $\pm 2S\text{Bi}/\pi$ are indicated by the solid and dashed lines, respectively. In (a) the horizontal dotted lines show (34).

236 boundary layers. Solutions approaching this limit are displayed in Fig. 9. As \mathcal{S} is decreased, the
 237 yielded regions become strongly localized to the extrema of the slosh, and the plugs occupy the
 238 bulk of the plate, which consequently remains largely straight. The narrow viscoplastic boundary
 239 layers at the troughs and crests correspond to the hinge points familiar in the theory of plastic
 240 plates [22,24]. In other words, in the perfectly plastic limit, the sloshing motion takes a distinctive,
 241 triangular wave form, with the plate only yielding in hinges at the wave crests and troughs.

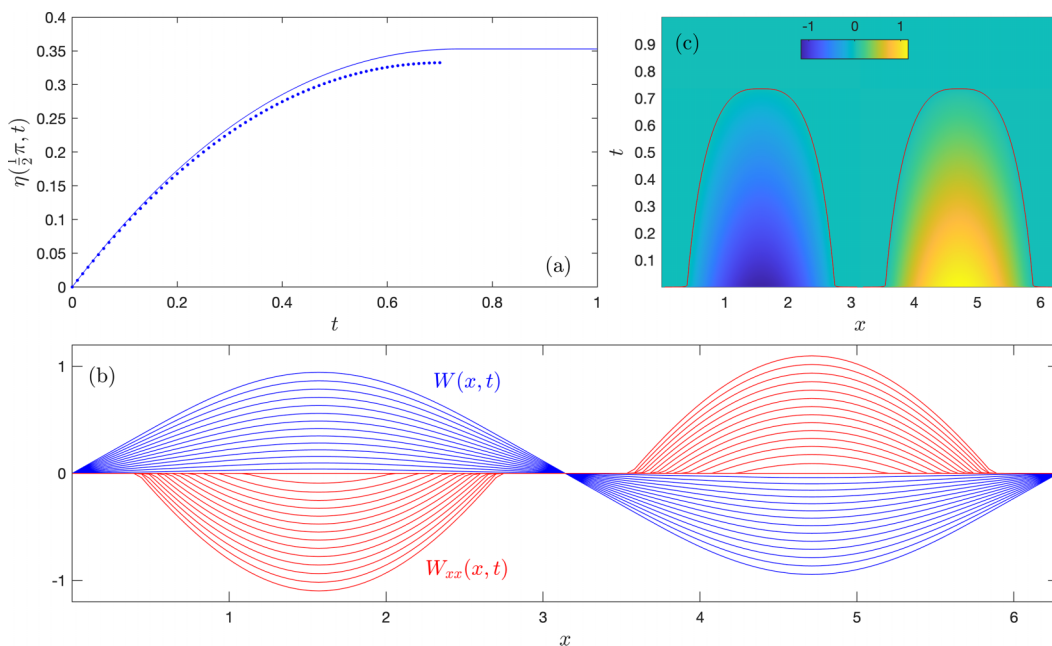


FIG. 7. Numerical solution for $\mathcal{S} = \frac{5}{2}$, $A_0 = 1$, $n = 1$, and $\text{Bi} = \frac{1}{2}$, plotting (a) time series $\eta(\frac{1}{2}\pi, t)$ and (b) equally spaced snapshots of $\eta(x, t)$ and $W_{xx}(x, t)$ at intervals of 0.05. In (a) the dots show the solution of (26). Panel (c) shows a density plot of the curvature rate W_{xx} , with the (red) contour showing the yield points.

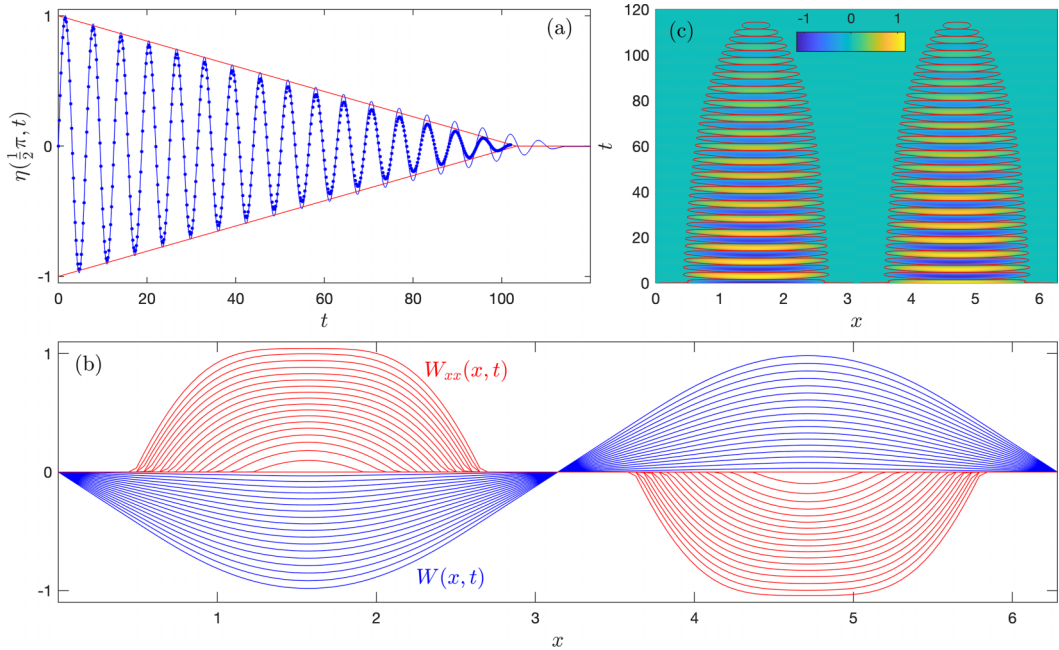


FIG. 8. Numerical solutions for a plate with $\mathcal{S} = 0.1$, $A_0 = \text{Bi} = 1$, and $n = 1$, plotting (a) time series $\eta(\frac{1}{2}\pi, t)$ and (b) snapshots of $\eta(x, t)$ and $W_{xx}(x, t)$ near the maxima of $A(t) = \eta(\frac{1}{2}\pi, t)$. In (a) the dots show the solution of (26) and the envelope of the decaying oscillations is $a \sim \pm A_0(1 - t/t_s)$. Panel (c) shows a density plot of the curvature rate W_{xx} , with the (red) contour showing the yield points.

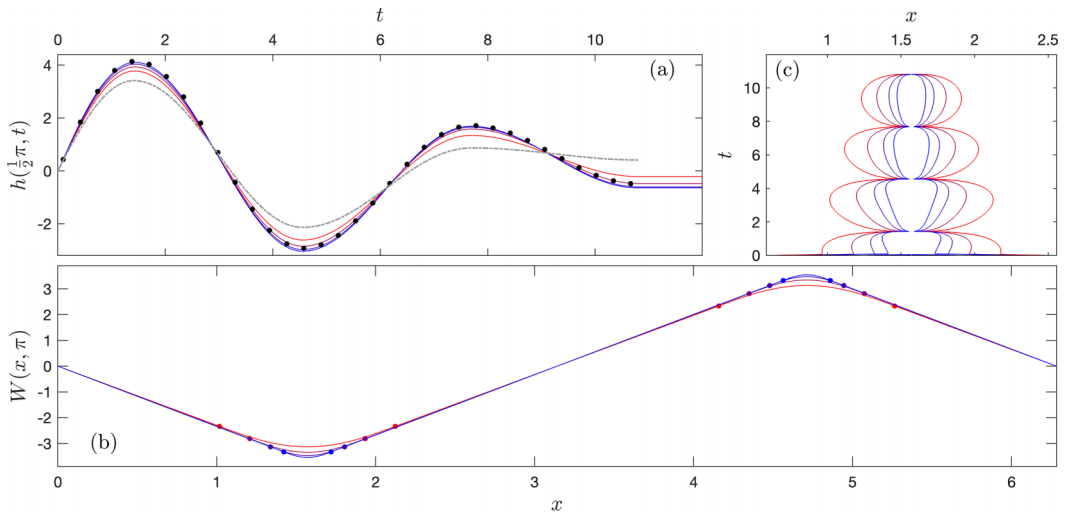


FIG. 9. Numerical solutions for $\mathcal{S} = 4^{-j} \times 0.04$, $j = 0, 1, 2, 3$, with $A_0 = 4$, $\mathcal{S}\text{Bi} = 1$, and $n = 1$ (color coded by the value of \mathcal{S} , from red to blue). Plotted are (a) the time series $\eta(\frac{1}{2}\pi, t)$ and (b) the snapshots $W(x, \pi)$. In (c) we show the positions of the yield points around $x = \frac{1}{2}\pi$ on the (x, t) plane. In (a) we also plot the prediction from (26) for $\mathcal{S} \rightarrow 0$ (gray dot-dashed), and the asymptotic result predicted by (38) (black dots), initializing that ODE at $t = t_i = 0.1$ with $A = \eta(\frac{1}{2}\pi, t_i)$ and $\dot{A} = W(\frac{1}{2}\pi, t_i)$ from the solution with the smallest value of \mathcal{S} , to remove the effect of initial transients. In (b) the yield points are highlighted.

242 The modification to the spatial structure of the solution indicates that the approximation of
 243 (26) cannot remain accurate as it relies on the separable solution in (25). Instead, we capture the
 244 triangular waveform for the plugged part of the plate in $0 \leq x \leq \frac{1}{2}\pi$, by writing

$$\eta \sim x\dot{\Gamma}, \quad W \sim x\dot{\Gamma}, \quad u \sim -\frac{1}{2}\dot{\Gamma}(x^2 - \frac{1}{4}\pi^2), \quad (35)$$

245 for some slope function $\Gamma(t)$ (given that $u_x = -W$ and $\int_0^{2\pi} u \, dx = 0$). The energy of the slosh,
 246 which primarily comes from the plugs, is therefore

$$4 \times \frac{1}{2} \int_0^{\frac{1}{2}\pi} (u^2 + \eta^2) \, dx \sim 4 \times \left(\frac{\pi^3 \dot{\Gamma}^2}{48} + \frac{\pi^5 \dot{\Gamma}^2}{480} \right). \quad (36)$$

247 The dissipation takes place exclusively over the hinges, however. The hinge in $0 \leq x \leq \frac{1}{2}\pi$, extends
 248 from $x = \frac{1}{2}\pi$, where $W_x = 0$, to a yield point $x = x_y$ that is a small distance to the left, where
 249 $W_x = \dot{\Gamma}$. Here, moreover, the bending moment is given chiefly by the (constant) plastic contribution,
 250 $M \sim -\frac{1}{2}\text{Bi} \, \text{sgn}(W_{xx}) \sim \frac{1}{2}\text{Bi} \, \text{sgn}(\dot{\Gamma})$. Hence, the energy equation (24) becomes

$$4 \times \frac{d}{dt} \left(\frac{\pi^3 \dot{\Gamma}^2}{48} + \frac{\pi^5 \dot{\Gamma}^2}{480} \right) \sim -4 \times \mathcal{S} \int_{x_y}^{\frac{1}{2}\pi} M W_{xx} \, dx \sim -4 \times \frac{1}{2} \mathcal{S} \text{Bi} |\dot{\Gamma}|, \quad (37)$$

251 which is equivalent to

$$\ddot{A} + \frac{10}{\pi^2} A + \frac{60}{\pi^4} \mathcal{S} \text{Bi} \, \text{sgn}(\dot{A}) \sim 0, \quad (38)$$

252 since $A \sim \frac{1}{2}\Gamma\pi$. As shown in Fig. 9(a), (38) provides an asymptotic solution for the slosh amplitude
 253 in the plastic limit that is superior to the approximation in (26). Note that, for the example shown
 254 in this figure, the perfectly plastic solution in (35) is not consistent with the initial condition
 255 (21), which prompts a rapid initial transient. To remove any effect of this initial adjustment, the
 256 figure displays the solution of (38) with initial values for (A, \dot{A}) matched to $(\eta(\frac{1}{2}\pi, t_i), W(\frac{1}{2}\pi, t_i))$
 257 from the numerical solution with the smallest values of \mathcal{S} at $t = t_i = 0.1$.

D. Power-law plate

258
 259 Finally, in Fig. 10 we show a solution for a power-law plate with $n = \frac{3}{5}$ ($\text{Bi} = 0$). As predicted
 260 by the approximate analysis based on the energy equation, the amplitude decays in finite time, with
 261 an envelope and stopping time t_s approximately given by (29). Despite this, the spatial structure of
 262 the solution departs from the separable form in (25), becoming noticeably flattened near the nodes,
 263 $x = 0, \pi, \dots$, where the effective viscosity diverges [Fig. 10(b)].

264 Note that, for weakly damped solutions of the kind shown in Fig. 10 (with $\mathcal{S} \ll 1$),

$$\eta(x, t) \sim A(t) \sin x + \delta^3 N(\xi, t), \quad \delta = \mathcal{S}^{\frac{1}{5-n}}, \quad (39)$$

265 where $N(\xi, t)$ is a function that is localized to the nodes, $x = j\pi$, $j = 0, 1, \dots$, and depends on
 266 the finer spatial scale, $\xi = \delta^{-1}(x - j\pi)(-1)^j$. This structure is demanded by the main balance of
 267 terms,

$$N_{\xi\xi\xi} \sim (|N_{\xi\xi t}|^n)_{\xi\xi\xi\xi\xi}, \quad (40)$$

268 which descends from (20) and (19), and the need to suppress the curvature rate, $W_{xx} \sim -A(t) \sin x +$
 269 $\delta N_{\xi\xi\xi} \sim \delta \xi A + \delta N_{\xi\xi\xi}$, as $x \rightarrow j\pi$ [cf. Fig. 10(b)]. These scalings imply that $\eta - A \sin x$ and $W_{xx} +$
 270 $\dot{A} \sin x$ should scale as δ^3 and δ , respectively, as demonstrated in Fig. 10(c) for a suite of com-
 271 putations with varying \mathcal{S} . The convergence to the undamped limit is therefore relatively slow
 272 and its details are convoluted [requiring the solution to (40)]. With finite Bi, the weakly damped
 273 solutions have a somewhat similar form, although the structure is further modified and complicated
 274 by the need to eliminate W_{xx} at the moving boundaries of the plugs surrounding each node (see

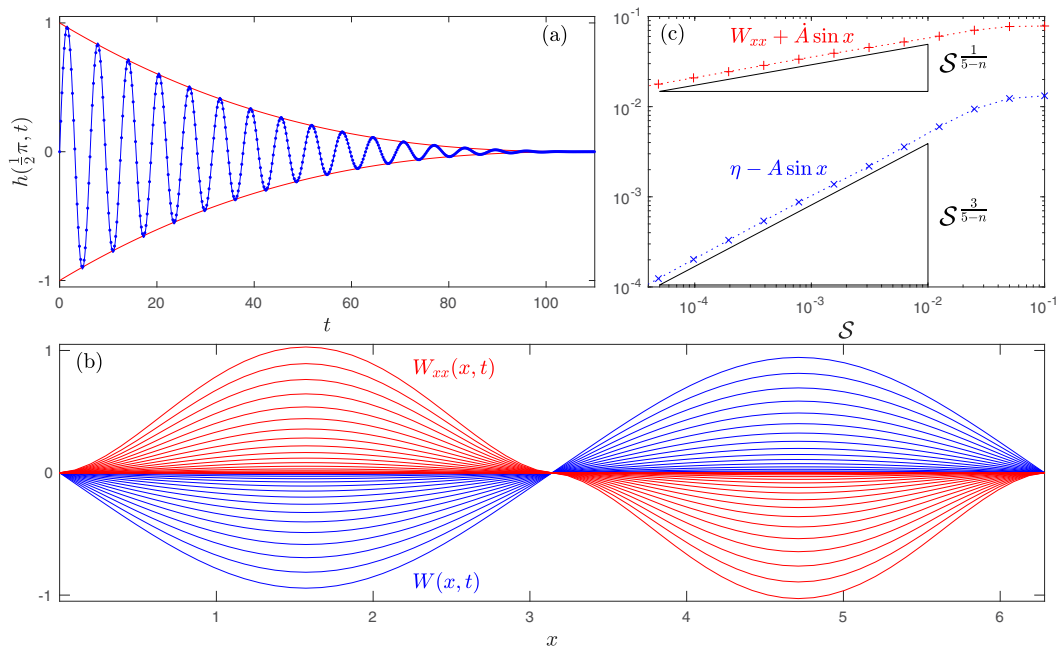


FIG. 10. Numerical solutions for a power-law plate with $\mathcal{S} = 0.1$, $A_0 = 1$, $\text{Bi} = 0$, and $n = \frac{3}{5}$, plotting (a) time series $\eta(\frac{1}{2}\pi, t)$ and (b) snapshots of $\eta(x, t)$ and $W_{xx}(x, t)$ near the maxima of $A(t) = \eta(\frac{1}{2}\pi, t)$. In (a) the dots show the solution of (26) and the envelope of the decaying oscillations is the prediction in (29). Panel (c) shows scalings data for a suite of solutions with varying \mathcal{S} , plotting the maximum values of $\eta - A \sin x$ and $W_{xx} + \dot{A} \sin x$, averaged over the oscillation for $\frac{1}{2}\pi < t < \frac{5}{2}\pi$. Also indicated are $\delta = \mathcal{S}^{\frac{1}{5-n}}$ and $\delta^3 = \mathcal{S}^{\frac{3}{5-n}}$.

Fig. 8). Overall, mapping out the passage of the model to the undamped water-wave limit is not a straightforward exercise.

IV. CONCLUSION

In this paper, we have explored the damping of standing surface waves by the bending of a thin, floating film of yield-stress fluid. For this task, we coupled the shallow-water equations for an inviscid layer of water with a model for the bending of an overlying viscoplastic plate, implying a long-wavelength approximation for both the waves and the floating film. The analysis can be easily extended to consider propagating waves. Moreover, as we demonstrate in the Appendix, the assumption that the water layer is shallow is not key: the model can be straightforwardly generalized to study the damping of irrotational surface waves on a water layer of arbitrary depth, assuming only that surface displacements are of order the plate thickness (which is again taken to be small in comparison to the wavelength).

The model predicts that sloshing motions corresponding to standing waves become arrested in finite time by the yield stress, somewhat like how layers of floating particles have been observed to impact seiches in a rectangular tank [7,8]. For a viscoplastic plate, however, the yield stress leads to a linear decrease in wave amplitude with time. By contrast floating hydrogel or polystyrene appears to prompt a weaker decay in which the wave amplitude decreases as a power law, $(t_s - t)^\alpha$, with an exponent α between 2 and 3 (t_s being the stopping time). As we have noted, a weaker decay of the wave amplitude can be achieved when the plate has a shear-thinning power-law viscosity and no yield stress (the constitutive behavior being described by the Herschel-Bulkley model). Although it is conceivable that a suspension of hydrogel spheres or polystyrene particles could behave like

296 a single-phase, shear-thinning complex fluid, it seems more likely that the dynamical dilation and
 297 compaction of the floating particle pack during the cycle of the sloshing motions plays a key role in
 298 setting the rate of decay. In particular, since the local volume fraction of solid sets the effective yield
 299 stress, the dilation of the particle pack may weaken the effect of plastic bending until sloshing has
 300 largely subsided and the particles may once more jam. An incorporation of such dynamics requires
 301 a two-phase description.

302 APPENDIX: NONSHALLOW SLOSHING

303 When the lower layer is not shallow, we cannot use the reduction in Sec. II B for that region.
 304 Instead, we follow the quasilinear approximation of Sec. II E with $\epsilon = O(1)$ and $\delta \ll 1$. The
 305 plate model then remains unchanged and we may deal with the inviscid lower layer by following
 306 conventional water-wave theory and assuming potential flow. Therefore, if $(u, w) = \nabla\phi$, where ϕ
 307 is the velocity potential, we have

$$\left. \begin{aligned} \epsilon^2\phi_{xx} + \phi_{xx} = 0, \quad \phi_z(x, 0, t) = 0, \quad \begin{cases} \epsilon^2\eta_t - \phi_z = 0 \\ \phi_t + \eta + SP = 0 \end{cases} \end{aligned} \right\} \text{on } z = 1, \quad (\text{A1})$$

308 after removing all dimensions as in Sec. II D (with the additional scalings of z by \mathcal{H} , w by $\mathcal{D}\mathcal{C}/\mathcal{L}$ and
 309 ϕ by $\mathcal{D}\mathcal{C}\mathcal{L}/\mathcal{H}$), and linearizing the interfacial boundary conditions about the undisturbed surface,
 310 $z = 1$. We may solve (A1) with the use of a Fourier series, to find

$$\eta_{tt} = -\frac{1}{\epsilon\pi} \sum_{j=1}^{\infty} j \tanh \epsilon j \sin jx \int_0^{2\pi} (\eta + SP) \sin j\hat{x} d\hat{x}, \quad (\text{A2})$$

311 in place of (20). Consequently, although some of the simplicity of the quasilinear equations in
 312 Sec. II E are lost, the model remains similar outside the shallow limit [the second derivative ∂_x^2 in
 313 (20) being replaced by the integral operator in (A2)]. In particular, the energy equation correspond-
 314 ing to (24) is

$$\frac{d}{dt} \int_0^{2\pi} \left[\frac{1}{2} \eta^2 dx + \int_0^1 \frac{1}{2} (\phi_x^2 + \epsilon^{-2} \phi_z^2) dz \right] dx = -\mathcal{S} \int_0^{2\pi} \left[(n+2)^{-1} |W_{xx}|^n + \frac{1}{2} \text{Bi} \right] |W_{xx}| dx, \quad (\text{A3})$$

315 and, but for the change to some algebraic factors (associated with a different form for the kinetic
 316 energy of the sloshing motions), the approximate solution in Sec. III A and the asymptotic plastic

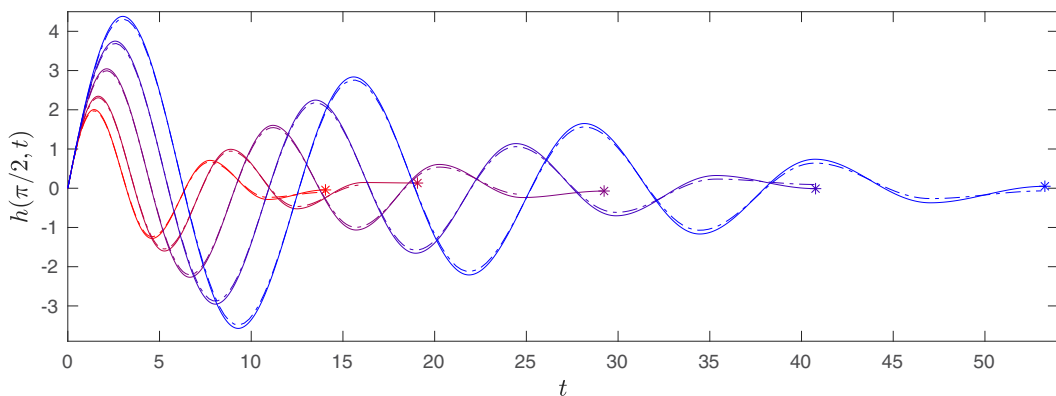


FIG. 11. Numerical solutions for a Bingham plate with $\mathcal{S} = \text{Bi} = \frac{1}{2}$, and $A_0 = 1$, above a nonshallow water layer with varying ϵ . Plotted are time series of $\eta(\frac{1}{2}\pi, t)$ (solid) along with predictions from (A4) (dot-dashed), with $\epsilon = 0.1, 1, 2, 3$, and 4 (from red to blue). Motion ceases at the times indicated by stars.

solution of Sec. III C are unchanged. For example, (33) is replaced with

$$\frac{\epsilon \ddot{A}}{\tanh \epsilon} + A + \frac{1}{2} S \dot{A} + \frac{2S\text{Bi}}{\pi} \text{sgn}(\dot{A}) = 0. \quad (\text{A4})$$

Numerical solutions employing (A2) in place of (20) (and using a corresponding spectral scheme) also demonstrate that there is no qualitative change to the dynamics captured by the model. Some sample solutions are shown in Fig. 11. The main effect of reducing the aspect ratio of the water layer (i.e., increasing ϵ) is to increase the inertia of the slosh, and therefore the damping time.

-
- [1] V. A. Squire, A fresh look at how ocean waves and sea ice interact, *Phil. Trans. R. Soc. A* **376**, 20170342 (2018).
- [2] V. A. Squire, Ocean wave interactions with sea ice: A reappraisal, *Annu. Rev. Fluid Mech.* **52**, 37 (2020).
- [3] P. Behroozi, K. Cordray, W. Griffin, and F. Behroozi, The calming effect of oil on water, *Am. J. Phys.* **75**, 407 (2007).
- [4] G. Sutherland, T. Halsne, J. Rabault, and A. Jensen, The attenuation of monochromatic surface waves due to the presence of an inextensible cover, *Wave Motion* **68**, 88 (2017).
- [5] A. Sauret, F. Boulogne, J. Cappello, E. Dressaire, and H. A. Stone, Damping of liquid sloshing by foams, *Phys. Fluids* **27**, 022103 (2015).
- [6] C. Zhang, P. Su, and D. Ning, Hydrodynamic study of an anti-sloshing technique using floating foams, *Ocean Eng.* **175**, 62 (2019).
- [7] B. R. Sutherland and N. J. Balmforth, Damping of surface waves by floating particles, *Phys. Rev. Fluids* **4**, 014804 (2019).
- [8] V. A. Kalinichenko, Suppression of intense fluid oscillations by a floating particle layer, *Fluid Dyn.* **55**, 804 (2020).
- [9] F. Viola, P.-T. Brun, B. Dollet, and F. Gallaire, Foam on troubled water: Capillary induced finite-time arrest of sloshing waves, *Phys. Fluids* **28**, 091701 (2016).
- [10] F. Viola and F. Gallaire, Theoretical framework to analyze the combined effect of surface tension and viscosity on the damping rate of sloshing waves, *Phys. Rev. Fluids* **3**, 094801 (2018).
- [11] F. Viola, P.-T. Brun, and F. Gallaire, Capillary hysteresis in sloshing dynamics: A weakly nonlinear analysis, *J. Fluid Mech.* **837**, 788 (2018).
- [12] B. Dollet, É. Lorenceau, and F. Gallaire, Transition from Exponentially Damped to Finite-Time Arrest Liquid Oscillations Induced by Contact Line Hysteresis, *Phys. Rev. Lett.* **124**, 104502 (2020).
- [13] N. J. Balmforth and R. V. Craster, Ocean waves and ice sheets, *J. Fluid Mech.* **395**, 89 (1999).
- [14] I. Cheddadi, P. Saramito, C. Raufaste, P. Marmottant, and F. Graner, Numerical modelling of foam Couette flows, *Eur. Phys. J. E* **27**, 123 (2008).
- [15] R. Salmon, *Lectures on Geophysical Fluid Dynamics* (Oxford University Press, New York, 1998).
- [16] N. J. Balmforth and I. J. Hewitt, Viscoplastic sheets and threads, *J. Non-Newtonian Fluid Mech.* **193**, 28 (2013).
- [17] N. J. Balmforth, I. A. Frigaard, and G. Ovarlez, Yielding to stress: Recent developments in viscoplastic fluid mechanics, *Annu. Rev. Fluid Mech.* **46**, 121 (2014).
- [18] T. V. Ball and N. J. Balmforth, Viscoplastic plates, *Proc. R. Soc. A* **477**, 20210509 (2021).
- [19] P. D. Howell, Models for thin viscous sheets, *Eur. J. Appl. Math.* **7**, 321 (1996).
- [20] N. M. Ribe, Bending and stretching of thin viscous sheets, *J. Fluid Mech.* **433**, 135 (2001).
- [21] N. M. Ribe, A general theory for the dynamics of thin viscous sheets, *J. Fluid Mech.* **457**, 255 (2002).
- [22] W. Prager and P. G. Hodge, *Theory of Perfectly Plastic Solids* (Wiley, 1951).
- [23] P. G. Hodge Jr. and T. Belytschko, Numerical methods for the limit analysis of plates, *J. Appl. Mech.* **35**, 796 (1968).
- [24] J. Lubliner, *Plasticity Theory* (Courier Corporation, 2008).
- [25] L. N. Trefethen, *Spectral Methods in MATLAB* (SIAM, 2000).